# LatentDreamer: Single Image to High-Quality 3D Object via Latent Features

Huanning Dong<sup>a</sup>, Yinuo Huang<sup>a</sup>, Fan Li<sup>a,\*</sup>, Ping Kuang<sup>a</sup>

<sup>a</sup>University of Electronic Science and Technology of China, Chengdu, China

### Abstract

3D assets are essential in the digital age. While automatic 3D generation, such as image-to-3d, has made significant strides in recent years, it often struggles to achieve fast, detailed, and high-fidelity generation simultaneously. In this work, we introduce LatentDreamer, a novel framework for generating 3D objects from single images. The key to our approach is a pre-trained variational autoencoder that maps 3D geometries to latent features, which greatly reducing the difficulty of 3D generation. Starting from latent features, the pipeline of LatentDreamer generates coarse geometries, refined geometries, and realistic textures sequentially. The 3D objects generated by LatentDreamer exhibit high fidelity to the input images, and the entire generation process can be completed within a short time (typically in 70 seconds). Extensive experiments show that with only a small amount of training, LatentDreamer demonstrates competitive performance compared to contemporary approachs.

Keywords: Image-to-3D, Mesh Generation, Variational Autoencoder

### 1. Introduction

Currently, 3D models are widely used in extensive applications, such as video gaming, animation, education, virtual reality and augmented reality. However, the production of high-fidelity 3D contents often remains a labor-intensive task. Recently, advances in generative AI have shown substantial potential for automatic 3D content generation. For instance, DreamFusion [1]

<sup>\*</sup>Corresponding author



Figure 1: **Result of our method.** Our method can generate high-quality textured 3D objects from single images in **70 seconds**. Input images (along with text prompts), normal maps of the generated objects, and multi-view color images are shown.

employs a pretrained 2D text-to-image diffusion model and the score distillation sampling (SDS) loss to optimize a neural radiance field [2] (NeRF). However, such methods are usually time-consuming (DreamFusion takes about 30 minutes to generate a model), as the rendering process of NeRF is slow. Moreover, SDS, as prior knowledge for text-to-image tasks, is prone to the multi-face (Janus) problem due to the lack of explicit image constraints, making it unsuitable for image-to-3D tasks. To address this, some recent studies [3, 4, 5, 6, 7, 8, 9] focus on consistent multi-view images generation that advance image-to-3D development.

Another line of works [10, 11, 12, 13, 14, 15, 16] investigate the use of diffusion models [17] to generate 3D content directly. They typically train diffusion models on 3D datasets to generate 3D objects or their intermediate representations. The essence of diffusion-based methods is an iterative denoising process that uses the output of a network (e.g., U-Net [18]) as a guide for each iteration. Such methods face several inherent challenges, including slow generation speed, lack of details, and low fidelity to input prompts. Concurrent studies, such as LRM [19], explore the potential of transformers [20] to perceive 3D space. While these feed-forward methods [21, 19, 22, 23, 24, 25, 26] enable faster generation, they depend on extensive training with large amounts of 3D data. However, the limited quantity and variety of public 3D datasets [27, 28, 29] currently hinders their development, leading to subpar generation quality.

In summary, current methods for generating 3D objects from single images have difficulty to balance several challenges: fast generation, accurate geometry, generalization to open categories, and the fidelity to input prompts. In this paper, we propose a novel 3D generation framework that simultaneously addresses the above challenges. First, our method innovatively trains a robust signed distance functions variational autoencoder [30] (SAE) to encode the discrete representation of the signed distance functions (SDFs) into a global latent features, effectively overcoming the difficulties of optimizing SDFs under sparse views. Notably, during training, we utilize a random geometry generator to create training data, achieving excellent generalization without relying on any public 3D datasets. Second, our approach includes an efficient pipeline for single-image to 3D generation: (1) applying the pretrained multi-view diffusion model [4] and ControlNet [31] to derive multiview priors from a single image; (2) training an end-to-end neural network to quickly predict the initialization of latent features; (3) iteratively optimizing latent features to generate coarse meshes; (4) sculpting surface details to create refined meshes; and (5) generating realistic textures for the meshes using view-aware loss. As illustrated in Figure 1, our method can produce high-quality 3D mesh from a single image in just 70 seconds, demonstrating exceptional balance in geometric detail, robustness, generation speed, and multi-category generalization.

In general, our contributions are summarized as follows:

- We innovatively train SAE that encoding 3D objects into continuous latent features, reducing the difficulty of optimizing 3D objects and enhancing the robustness of generation.
- We propose an efficient multi-step generation pipeline consists of a self-attention based latent features initialization network (LIN). Our pipeline allows high-quality mesh generation from a single image in 70 seconds.
- We introduce a random geometry generator when training the SAE and LIN, enabling open-world categories 3D generation without relying on any public 3D datasets.

### 2. Related Works

### 2.1. 3D generation by optimizing the representation

A direct 3D object generation approach is optimize their representations via network inference. Previous researches have explored various types of 3D representations, including meshes, NeRF [2], 3D Gaussians [32]. Certain methods [1, 33, 34, 35, 36, 37, 38, 39, 40, 41] for optimizing NeRF are prone to problems like floating artifacts or defective geometry in space due to the lack of clear geometric surfaces. In addition, it usually takes tens of minutes or even hours to optimize a NeRF-based model. As an efficient 3D representation, 3D Gaussian [32] offers real-time rendering capabilities. Some studies [42, 43, 44] focus on optimizing 3D Gaussians to generate 3D objects, achieving faster generation speeds and enhanced visualization. However, the realistic visual quality of the generated objects heavily depends on spherical harmonics. These objects often lack explicit geometric structures and surfaces, which hinders user interaction and presents challenges for further applications in gaming, metaverses, simulations, and other fields. There are also studies [45, 13, 46, 47, 48, 49, 50] that achieve clear geometry by optimizing meshes (or SDFs). However, these methods are highly dependent on the accuracy of prior knowledge, exhibit poor robustness, struggle with convergence, and are prone to geometric misalignment. In this work, we encode SDFs into continuous latent features, effectively reducing the difficulty of the optimization process.

### 2.2. Direct 3D generation

Another line of research directly generates 3D objects by training networks. Some studies [10, 11, 12, 13, 14, 15, 16] adapting the concept of 2D diffusion and train 3D diffusion models on 3D datasets. For example, SD-Fusion [11] and 3DGen [12] train 3D latent diffusion models [51] (LDM) to produce 3D objects, but they encounter challenges in generalizing to openworld category objects due to the limitations of the datasets. CRM [10] trains a diffusion model to produce CCM representations that incorporate geometric information from multi-view images for geometric reconstruction. Other feed-forward methods [21, 19, 22, 23, 24, 25, 26], such as LRM [19], train a large transformer decoder to project image features into a 3D tri-plane representation. LGM [22] use an asymmetric U-Net to map multi-view images into multi-view Gaussian features, which are subsequently interpreted and

fused into 3D Gaussians. These approaches enhance the speed of 3D object generation, reducing the generation time to under 10 seconds.

We iteratively optimize meshes instead of directly generating them because the results of direct generation highly depend on the priors learned from the datasets. However, 3D datasets remain limited compared to 2D datasets, making it challenging to handle categories that have not been previously encountered. Furthermore, direct generation methods often lack strong constraints from input prompts, leading to lower quality and fidelity of the generated objects.

### 2.3. Multi-view Diffusion Models

There are several fundamental issues associated with using score distillation sampling (SDS) as a prior, including over-smoothing and time inefficiency. LucidDreamer [43] identifies the cause of over-smoothing and proposes Interval Score Matching (ISM) to alleviate this issue. But the time-consuming problem still remains.

Recent studies [3, 4, 5, 6, 7, 8, 9] concentrate on generating consistent multi-view 2D images. For instance, Zero123 fine-tunes a large stable diffusion model [52] for conditional diffusion generation. Given an image and a target view (R,t), Zero123 predicts the RGB image from the new viewpoint. Zero123 often results in inconsistencies among the generated views. In contrast, Zero123++ [4] generates fixed six-view images, which improves consistency across multiple views. These studies provide accurate pixel-level guidance for optimization-based methods (in Sec 2.1) while effectively solving multi-face problem.

### 3. Methodology

In this section, we introduce LatentDreamer. The overview of our framework is shown in Figure 2. For single image inputs, we first utilize a pretrained 2D diffusion model [4] and a ControlNet [31] to generate multi-view priors (in Sec 3.2). Directly optimizing SDFs based on sparse multi-view priors is challenging. We train a SAE that encodes discrete SDFs into continuous latent features, reducing the difficulty of optimizing SDFs (in Sec 3.1). During mesh generation, we first train an end-to-end latent features initialization network (LIN) to predict the initial values of the latent features (in Sec 3.3). In Sec 3.4, we further employ two rounds of optimization

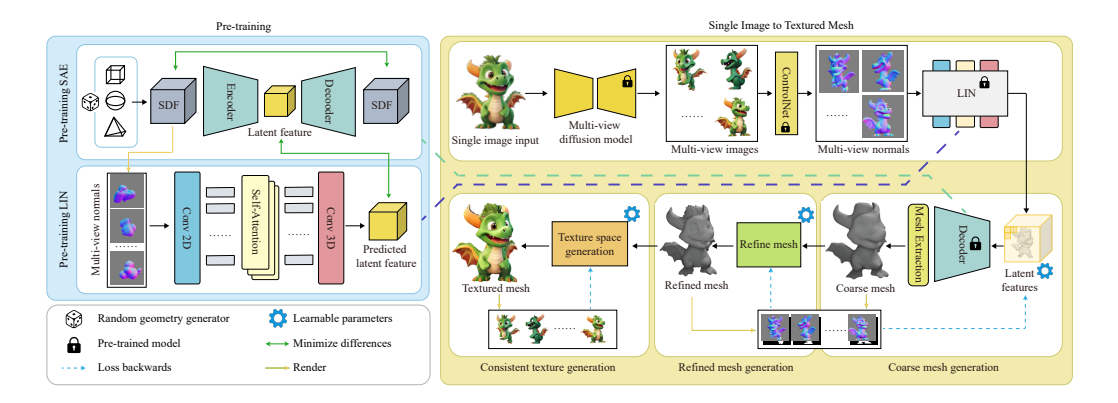


Figure 2: **Overview of LatentDreamer.** (Left) We pre-trained a SAE to decode SDF from latent features. Concurrently, we trained an end-to-end latent feature initialization network (LIN) to predict latent features from multi-view normals for rapid initialization. All training data is generated using a random geometry generator. (**Right**) For a single image input, LatentDreamer sequentially generates multi-view priors, initialized latent features, coarse mesh, refined mesh, and realistic mesh texture, with the entire process taking only 70 seconds to complete.

to generate coarse and refined meshes. Finally, in Sec 3.5, we introduce view-aware loss to generate realistic textures for meshes. Notably, we employed a random geometry generator during training to enhance the ability of both the SAE and LIN to handle various geometric shapes.

# 3.1. SAE for Any Geometry

Optimizing SDFs directly based on limited 2D guidance can lead to problems like geometric defects and surface holes, as illustrated in Figure 8 (w/o SDFs fixation). The generated geometry only fits the priors from limited views and lacks of completeness. To address this issue, we pre-train an SAE. The network structure of the SAE is built using 3D ResNet [53] layers. We train the encoder to convert discrete SDFs into global latent features. We find that optimizing latent features is easier than directly optimizing SDFs since the decoder is trained to recover latent features into geometry with complete and continuous surfaces. Experiments in Sec 4 have demonstrated that our approach is effective and robust.

The challenge of obtaining 3D training data is long-standing. We initially attempted to train SAE on public 3D datasets such as ShapeNet [27] and ModelNet [54]. While the model works well within the dataset classes, generating objects of unseen categories presents challenges. Therefore, we propose

a random geometry generator to train the SAE using randomly generated 3D geometries, instead of using any public 3D dataset. This strategy achieves impressive results. The decoder can reconstruct nearly any geometry from the latent features, as shown in Sec 4.4.

Random geometry generator. We assume that each random 3D geometry consists of n random blocks, each of which is described as:

$$S \in \mathbb{R}^3_{>0},$$
  
 $Block(S, P, R), \quad P \in \mathbb{R}^3_{>0},$   
 $R \in \mathbb{R}^3_{>0}$ 

Where S = (L, W, H) represents the shape of the block, P = (x, y, z) denotes the coordinate of the block's center, and  $R = (\theta_x, \theta_y, \theta_z)$  indicates the rotation of the block around its center. The above parameters (S, P, R) are all randomly generated. A random geometry is represented as:

$$Object3d_0 = \{Block_i(S_i, P_i, R_i) \mid i = 0, 1 \dots n\}$$
 (1)

To control the roundness of the geometry and the connections between blocks, we apply a random normalized Gaussian kernel to perform y rounds of blurring on each 3D geometry, defined as follows:

$$Object3d_{y+1} = F_{blur}(Object3d_y), y = 0, 1 \dots n - 1$$
(2)

Specifically, in each round of Gaussian blurring, the following calculations are performed for every coordinate in the space:

$$SDF'(\mathbf{x}) = \sum_{\mathbf{x'} \in \delta} SDF(\mathbf{x'}) \cdot G_{normalized}(\mathbf{x} - \mathbf{x'})$$
(3)

where

$$G_{normalized}(\boldsymbol{x}) = \frac{G(\boldsymbol{x})}{\sum_{\boldsymbol{x'} \in \delta} G(\boldsymbol{x'})}$$
(4)

$$G(\mathbf{x}) = \exp\left(-\frac{dist(\mathbf{x})^2}{2\sigma^2}\right) \tag{5}$$

Where  $\sigma$  is the radius of the Gaussian blur,  $\delta$  represents the area within the Gaussian kernel, while dist donates the distance between the coordinate and the center of the Gaussian kernel.  $\sigma$  and y are randomly generated in this process. For more details and results about random geometry generator, please refer to our supplement.

Loss function: In this work, we extract meshes from SDFs using Flexicubes [55], with its efficient and differentiable mesh extraction ability. Flexicubes defines the loss between the ground truth objects (gt-objs) and the predicted objects (pred-objs) as:  $\mathcal{L}_{flex} = \mathcal{L}_{render} + \mathcal{L}_{regularization} + \mathcal{L}_{SDF}$ . Here,  $\mathcal{L}_{render} = \mathcal{L}_{mask} + \mathcal{L}_{depth}$ . This component target to rasterize 3D geometry from the same viewpoint and minimize visual differences.  $\mathcal{L}_{regularization}$  is defined in Equations 8 and 9 of the paper [55] and focuses on the internal representation.  $\mathcal{L}_{SDF}$  regularizes the geometry by randomly sampling points in both gt-objs and pred-objs and minimizing the distance differences to their surfaces. We incorporated the general losses  $\mathcal{L}_{reconstruct}$  and  $\mathcal{D}_{KL}$  of VAE.  $\mathcal{L}_{reconstruct}$  measures the difference between the inputs and the outputs, here we use  $\mathcal{L}_2$  loss.  $\mathcal{D}_{KL}$  represents the difference between the latent features distribution and a known distribution, typically expressed as  $\mathcal{D}_{KL}(q(\mathbf{z}|\mathbf{x})||p(\mathbf{z}))$ .

We discard  $\mathcal{L}_{SDF}$  as sampling points and calculating surface distances are time-consuming, significantly reducing training efficiency. We test and find that this operation increases training speed without causing significant performance degradation. Moreover, we add  $\mathcal{L}_{normal}$  to  $\mathcal{L}_{render}$  to achieve more refined results by comparing the differences in multi-view normals. In general, we define the loss as follows (The coefficients are omitted):

$$\mathcal{L}_{V} = \mathcal{L}_{render} + \mathcal{L}_{regularization} + \mathcal{L}_{reconstruct} + \mathcal{D}_{KL}$$
 (6)

where

$$\mathcal{L}_{render} = \mathcal{L}_{mask} + \mathcal{L}_{depth} + \mathcal{L}_{normal} \tag{7}$$

# 3.2. Multi-view priors

In this work, we utilize Zero123++ [4] to obtain multi-view color images. Given a single input image, Zero123++ employs a pre-trained diffusion model to generate six-view RBG images with uniform azimuths and elevations of 20 and -10 degrees. We then use the pre-trained ControlNet [31] to predict the corresponding normals and further segment them to obtain masks. The

masks provide stronger constraints, facilitating the rapid derivation of the approximate 3D geometry. While the priors of six views are sparse for directly optimizing the SDFs, they are sufficient for latent features as discussed in Sec 3.1. Notably, since our 3D outputs are explicit meshes, it is straightforward to incorporate additional constraints, such as depth information. However, we refrain from using depth data because current monocular depth estimation methods [56, 57] do not yield accurate absolute depth information, which could result in incorrect geometry.

### 3.3. Initialization with Self-Attention

Through the encoding strategy discussed in Sec 3.1, we shift the focus of mesh generation from optimizing SDFs to optimizing latent features. However, optimizing geometry from scratch for each input is inefficient. To reduce the convergence time of latent features, we trained an end-to-end latent features initialization network (LIN) that takes multi-view normals as input and predicts the corresponding latent features of the target geometries. As shown in Figure 2, LIN first encodes the normals into low-dimensional features and then utilizes self-attention layers to obtain cross-view features. Finally, the latent features corresponding to the normals are predicted. The predicted value will serve as the initial value for the latent feature optimization process.

Similar to SAE, the training data for LIN is also generated by the random geometry generator (in Sec 3.1), which enhances its generalization ability. LIN is category-independent and focuses solely on the normals without recognizing the categories of the inputs. The loss of LIN is defined as the numerical difference between the predicted latent features and the target latent features (obtained from the encoder of the SAE), rather than the differences observed after rendering. Since latent features with different values may encode similar geometries, we consider that initializations with similar values are more appropriate. Quantitative experiments in Sec 4.5 demonstrate the efficacy of our design.

# 3.4. Single Image to Refined Mesh Generation

Although we pre-train SAE to compress SDFs into low-dimensional latent features, our approach does not incorporate the concept of latent diffusion models [51] (LDM) to train a diffusion model for generating these latent features, like SDFusion [11]. Because the latent features generated by the diffusion model lack sufficient accuracy, which diminishes the fidelity between decoded meshes and input images. Instead, we directly optimized the

latent features through gradient descent. Specifically, after obtaining the initial latent features  $\phi_0$  from the multi-view normals through LIN (Sec 3.3), a coarse-to-fine optimization process is employed to create refined meshes. First, we optimize the latent features iteratively to get coarse mesh, as follows:

$$\phi^* = \arg\min_{\phi} \mathbb{E}_{\theta}(R(F(D_{\xi}(\phi), d_0, w_0), \theta) - gt_{\theta})$$
(8)

Where  $D_{\xi}$  represents the decoder of the SAE, which decodes latent features  $\phi$  to SDFs. The initial value of  $\phi$  is given by the output  $\phi_0$  from LIN. Flexicubes [55] takes three parameters: SDF, Deform and Weight, and outputs the mesh.  $d_0$  and  $w_0$  are the default values of Deform and Weight. R denotes the differentiable rasterizer, while gt represents the multi-view priors obtained in Sec 3.2.  $\theta$  refers to the camera parameters. After this iteration, we obtain  $s^* = D(\phi^*)$ ,  $s^*$  is the approximate optimal value of SDFs which represents the coarse mesh. We then fix  $s^*$  and optimize Deform and Weight to carve the surface of mesh. The target is expressed as follows:

$$d^*, w^* = \underset{d,w}{\arg\min} \mathbb{E}_{\theta}(R(F(SDF_{out}, d, w), \theta) - gt_{\theta})$$
(9)

Overall, we obtain  $s^*, d^*, w^*$  as the approximate optimal values of SDF, Deform and Weight, and further get the refined mesh  $Mesh^* = F(s^*, d^*, w^*)$ . Our experiments in Sec 4.5 demonstrate that fixing  $s^*$  is crucial to avoid holes and misalignments caused by forced fitting. Throughout the mesh generation process, we render the normals and masks from multiple views and minimize the difference compared to the multi-view priors. The loss is represented as follows:

$$\mathcal{L}_G = \beta \mathcal{L}_{mask} + (1 - \beta) \mathcal{L}_{normal}, \beta \in (0, 1)$$
 (10)

We initially set  $\beta$  to a high value to quickly obtain a coarse shape, and then gradually reduce  $\beta$  to carve the details.

### 3.5. Consistent Texture Generation

We generate realistic textures by supervising the global texture space  $T(x), x \in \mathbb{Z}^3$ . For each vertex on the mesh, its color is determined by querying

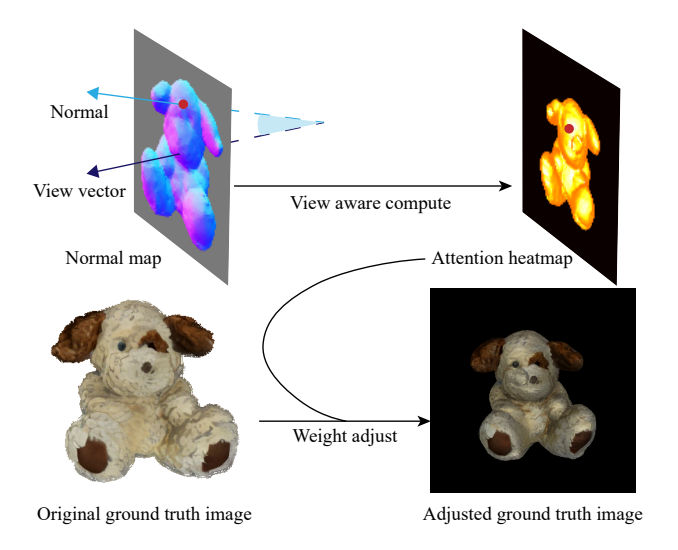


Figure 3: **View-aware loss.** We assign different weights to pixels based on the direction of their normals. In this figure, brighter points indicate higher weights for those pixels.

the nearest value in the texture space and performing trilinear interpolation. Using differentiable rasterization [58], we render multi-view RGB images, compare them with the prior multi-view RGB images (in Sec 3.2), and backpropagate the gradient to the texture space. Since the generated prior multi-view RGB images may exhibit inconsistencies, we design a view-aware loss to mitigate potential texture ghosting. The loss is based on the angle between the viewing vector and the surface normal, focusing on the texture loss from critical viewpoints. The general process is illustrated in Figure 3. With this approach, we obtain realistic and natural textures even in areas where multiple views overlap. The design of our texture loss is as follows:

$$\mathcal{L}_t(x,y) = \begin{cases} 0, & \text{if } \cos(\mathbf{v}_i, \mathbf{n}_{x,y}) \le 0\\ (\Delta C_{x,y})^2 \cdot \cos(\mathbf{v}_i, \mathbf{n}_{x,y})^k, & \text{else} \end{cases}$$
(11)

Where x, y are 2D coordinates,  $\Delta C$  represents the difference between the prior RGB image and the rendered RGB image,  $\mathbf{v}_i$  is the current viewing vector,  $\mathbf{n}_{x,y}$  is the normal vector at the coordinate, and k is a hyperparameter that adjusts the degree of view awareness.

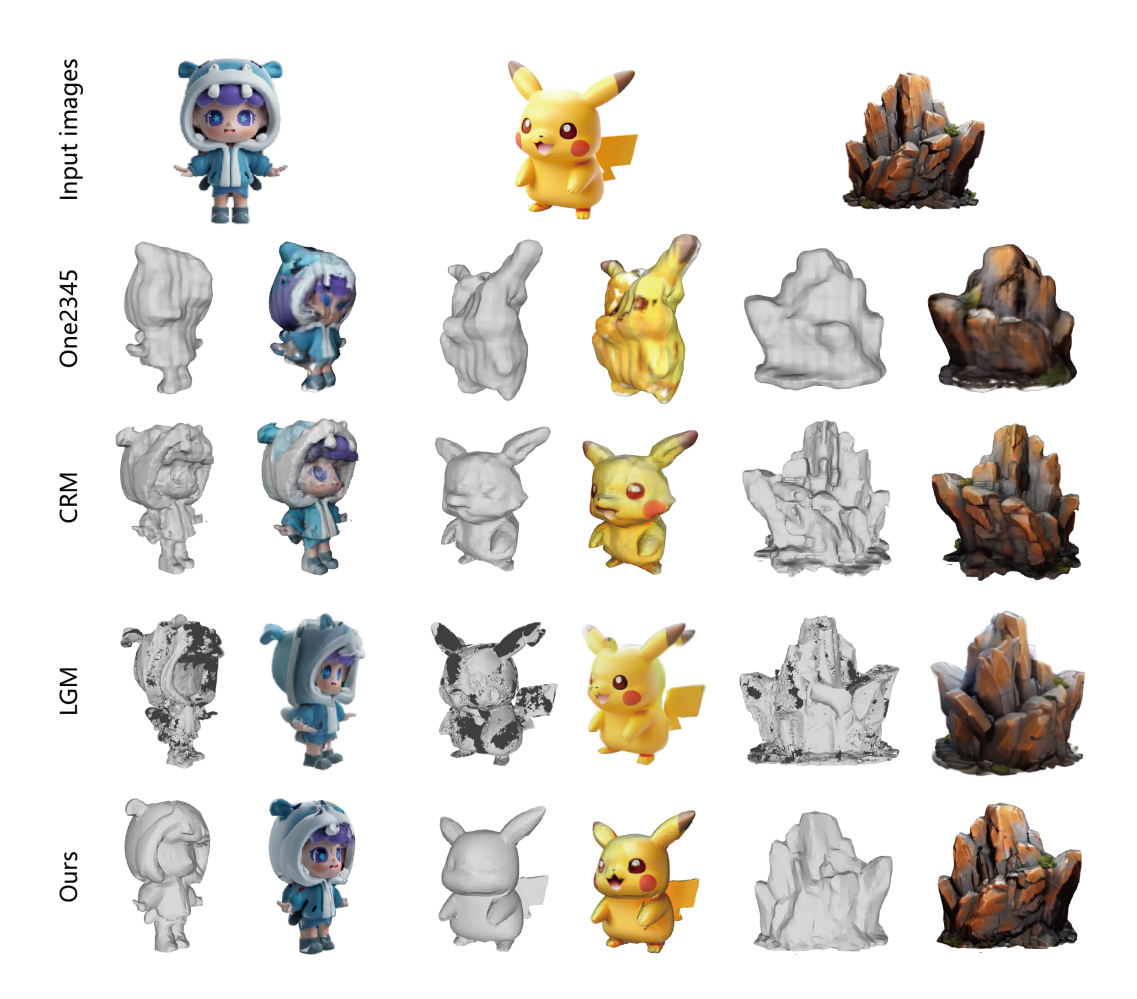


Figure 4: Comparison in single-image-to-3D generation. Input images, meshes, and rendering RGB results are shown. The 3D representation of LGM [22] is 3D Gaussians, from where we obtain its rendering results. The other rendering results are derived from the textured mesh. Zoom-in for details.

# 4. Experiments

### 4.1. Implementation Details

We set the SDFs size to 64<sup>3</sup> and the texture space to 260<sup>3</sup>. Before generation process, we apply rambg [59] for background segmentation to focus on the target object. After mesh generation in Sec 3.4, we employ loop subdivision [60] to increase the density of the mesh vertices, allowing for more detailed texture rendering. Notably, the entire training process of LatentDreamer can be completed within two days on a single RTX 3090 GPU without using public 3D datasets, highlighting the efficiency and potential of our method.

## 4.2. Qualitative Results

Single image to 3D generation. We compare our method for generating 3D objects from single images with several existing 3D generation methods, including Shap-E [14], One2345 [21], LGM [19], CRM [10], and OpenLRM [19, 61]. Qualitative results are presented in Figures 4 5. The examples in Figure 5 are sourced from GSO [62], providing a general reference. Figure 4 displays the untextured mesh and RGB rendering results. However, we only present the multi-view rendering results in Figure 5, since some methods, such as OpenLRM, utilize implicit representations and report only the rendering outcomes.

Among these methods, One2345 can only capture approximate appearances of the objects, resulting in overly smooth outputs. Shap-E can generate 3D objects with styles similar to the input images. However, it often struggles to maintain fidelity to the input images. CRM utilizes a diffusion model to generate intermediate representations, from which it subsequently extracts meshes. However, the resulting meshes exhibit uneven surfaces. LGM employs 3D Gaussians as its 3D representation, which may result in incorrect geometry, such as duplicated Pikachu ears (in Figure 4). OpenLRM use NeRF representation, frequently resulting in distorted geometry and exhibiting impressive visual quality only from the input perspective. In comparison, our method outperforms the above methods in terms of texture detail, fidelity of output results to input images, and overall geometric quality.

Text to 3D generation. In addition to generating high-fidelity 3D objects from single images, LatentDreamer can also be combined with main-stream text-to-image frameworks (e.g. Stable Diffusion[52], DALL-E[63]) to



Figure 5: Qualitative results on GSO [62]. The 3D objects generated by our method exhibit significantly better fidelity and are free from geometric flattening and distortion.

generate creative and imaginative 3D contents from text descriptions, such as "A penguin made of sweater" in Figure 1.

### 4.3. Quantitative Results

Comparison with Baselines. We select Point-E [64], Shap-E [14], LGM [19], OpenLRM [19, 61], and Zero123 [3] as baseline methods for quantitative comparisons. Zero123 can generate multi-view images from arbitrary viewpoints based on a single image and can be combined with SDS loss for 3D generation. We utilize the ThreeStudio [65] implementation for Zero123 and the official implementations for the other methods. Our quantitative comparisons are conducted on 200 objects from GSO [62]. For each object, we render a 512×512 color image of the generated result and compare it with the input image. The results are presented in Table 1, where we report CLIP [66] similarity, PSNR, SSIM [67], and LPIPS [68]. Since OpenLRM [19, 61] and Point-E [64] also report mesh results, we compare the geometry generation quality with them, as shown in Table 2. We align the center of generated meshes to zero, carefully adjust the scale and pose of the meshes. And then calculate Chamfer Distance, Volume IoU and F-score with the ground truth

Method	CLIP-Sim↑	PSNR↑	SSIM↑	LPIPS↓
point-E[64]	0.956	17.950	0.893	0.127
shap-E[14]	0.872	16.758	0.892	0.189
LGM[22]	0.963	21.420	0.910	0.078
OpenLRM[19, 61]	0.956	17.938	0.893	0.128
Zero123[3]	0.897	18.957	0.896	0.123
Ours	0.966	21.515	0.914	0.059

Table 1: Quantitative results of the image rendering quality. These results are evaluated on 200 objects in GSO [62]. Best values are highlighted in bold.

Method	Chamfer Dist↓	Volume IoU↑	F-score(%)↑
point-E[64]	0.0188	0.175	64.29
OpenLRM[19, 61]	0.0176	0.316	55.08
Ours	0.0084	$\boldsymbol{0.525}$	71.16

Table 2: Quantitative results of the geometry generation quality. Among them, we set the resolution for volumetric IoU computation to 128, and the threshold for the F-score to 0.05. Best values are highlighted in bold.

meshes. Both the image rendering results and the geometry quality results show the competitiveness of our method.

User study. We provide single images as inputs and reconstruction results as output, asking users to evaluate the consistency score (cs), geometric quality score (gs), and rendering score (rs). A total of 1380 sets of results were collected from 46 users. The statistical results are presented in Table 3, where we report the average ranking and total average scores for the three metrics. Overall, our method is preferred by the majority of users.

## 4.4. Analysis

Reasons for strong multi-category generalization ability. Through the SAE described in Sec 3.1, we encode meshes into latent features that contain a compact amount of data (set to 4096 numbers). These features can represent most geometric shapes well. The experimental results are illustrated in Figure 6.

Our experimental inputs include geometries of varying sizes, multiple separate geometries, and geometries with complex surfaces. The results

Method	csRank↓	gsRank↓	rsRank↓	avgScore†
shap-E[14]	4.630	4.565	4.696	10.861
One2345[21]	4.478	4.696	4.326	11.085
LGM[22]	2.782	2.717	2.457	16.488
OpenLRM[19, 61]	3.935	3.696	3.783	13.429
Ours	1.630	2.022	2.109	18.631

Table 3: Statistical results of evaluations from 46 participants. Higher scores and lower rankings are better. Our method leads in rankings of various metrics and overall performance.

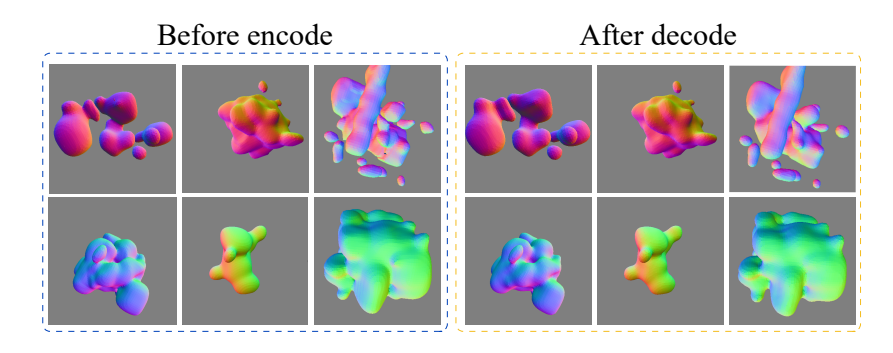


Figure 6: **Result of SAE.** The left side displays the normals of the input geometries, while the right side shows the normals of the geometries generated by the decoder.

demonstrate that our encoder—decoder framework effectively compresses and reconstructs arbitrary geometric shapes. The decompressed shapes closely resemble the original inputs while exhibiting smoother surfaces. According to our measurements, the Volume IoU between the input and output geometries can exceed 0.90. The generation of geometric shapes relies entirely on the guidance of latent space optimization and is independent of the object category.

### 4.5. Ablation studies

Several key strategies are used in LatentDreamer, including latent features initialization, SDFs fixation and mesh refinement. In this section, we verify the effectiveness of these designs through experiments.

Latent Features Initialization Network (LIN). In this section, we conducted comparative experiments to demonstrate the efficacy of LIN mentioned in Sec 3.3. The quantitative results are presented in Figure 7 and

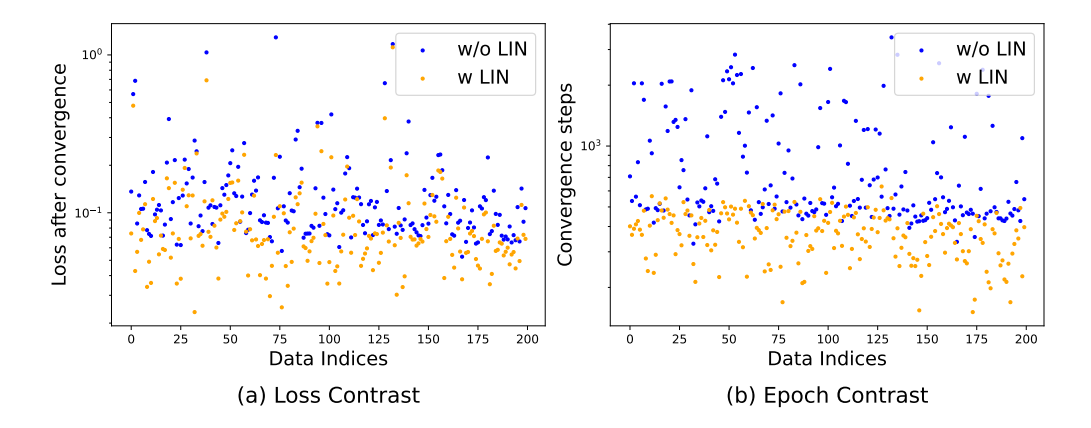


Figure 7: Comparison result of whether to use LIN. (a) The loss after the generation process converges. (b) The number of iterations required for convergence.

LIN	epoch (avg)↓	loss (avg)↓	SD (epoch)↓
w/o	884.83	$0.1462 \\ 0.0955$	628.08
w/	374.03		95.78

Table 4: **Statistical results of whether to use LIN.** Smaller value is better. SD(epoch) measures the stability of the generation process.

Table 4. Our experiments were performed on 200 objects from GSO [62].

Through pre-trained LIN, we can quickly get a suitable initialization of latent features. The convergence time is greatly shortened and the final generation quality is also improved, demonstrating that a suited initialization can prevent the model from getting trapped in a local optimum. Additionally, the gradient descent of the initialized model is more stable, ensuring convergence in a short time.

**SDF Fixation and Mesh Refinement.** After optimizing latent features to generate coarse meshes, we iteratively refine the *Deform* and *Weight* parameters of the Flexicubes [55] to sculpt geometric surface details while fixing the SDFs to prevent geometric defects (in Sec 3.4). Qualitative results are illustrated in Figure 8, highlighting the effectiveness and necessity of our design. Our approach enables the generation of complete and detailed geometries.

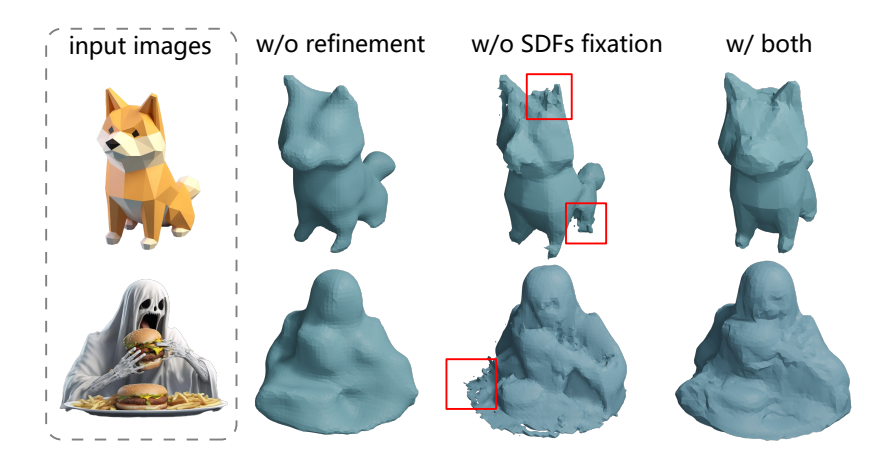


Figure 8: Ablation study results of whether to use our strategies. From left to right: input images, mesh generation without mesh refinement, without SDFs fixation, and with the complete strategy.

### 5. Conclusions

In this paper, we present LatentDreamer, an innovative method for generating 3D textured meshes from single images. Compared to existing methods, LatentDreamer offers several advantages, including high-quality geometry with detailed surfaces, realistic textures, strong fidelity to the original input image, and efficient generation (typically in 70 seconds). The outstanding performance of LatentDreamer indicates broad application prospects, such as generating 3D objects from personalized text descriptions and controllable 3D character animation. Furthermore, the random geometry generator we propose in this paper can provide a viable solution to the persistent challenges of limited 3D data availability and accessibility.

#### References

- [1] B. Poole, A. Jain, J. T. Barron, B. Mildenhall, Dreamfusion: Text-to-3d using 2d diffusion, arXiv (2022).
- [2] B. Mildenhall, P. P. Srinivasan, M. Tancik, J. T. Barron, R. Ramamoorthi, R. Ng, Nerf: Representing scenes as neural radiance fields for view synthesis, in: ECCV, 2020.
- [3] R. Liu, R. Wu, B. V. Hoorick, P. Tokmakov, S. Zakharov, C. Vondrick, Zero-1-to-3: Zero-shot one image to 3d object (2023). arXiv:2303.11328.

- [4] R. Shi, H. Chen, Z. Zhang, M. Liu, C. Xu, X. Wei, L. Chen, C. Zeng, H. Su, Zero123++: a single image to consistent multi-view diffusion base model (2023). arXiv:2310.15110.
- [5] X. Long, Y.-C. Guo, C. Lin, Y. Liu, Z. Dou, L. Liu, Y. Ma, S.-H. Zhang, M. Habermann, C. Theobalt, et al., Wonder3d: Single image to 3d using cross-domain diffusion, arXiv preprint arXiv:2310.15008 (2023).
- [6] Y. Liu, C. Lin, Z. Zeng, X. Long, L. Liu, T. Komura, W. Wang, Sync-dreamer: Generating multiview-consistent images from a single-view image (2024). arXiv:2309.03453.
  URL https://arxiv.org/abs/2309.03453
- Y. Lu, J. Zhang, S. Li, T. Fang, D. McKinnon, Y. Tsin, L. Quan, X. Cao,
   Y. Yao, Direct2.5: Diverse text-to-3d generation via multi-view 2.5d diffusion (2024). arXiv:2311.15980.
   URL https://arxiv.org/abs/2311.15980
- [8] M. Liu, R. Shi, L. Chen, Z. Zhang, C. Xu, X. Wei, H. Chen, C. Zeng, J. Gu, H. Su, One-2-3-45++: Fast single image to 3d objects with consistent multi-view generation and 3d diffusion, arXiv preprint arXiv:2311.07885 (2023).
- [9] Y. Shi, P. Wang, J. Ye, L. Mai, K. Li, X. Yang, Mvdream: Multi-view diffusion for 3d generation, arXiv:2308.16512 (2023).
- [10] Z. Wang, Y. Wang, Y. Chen, C. Xiang, S. Chen, D. Yu, C. Li, H. Su, J. Zhu, Crm: Single image to 3d textured mesh with convolutional reconstruction model, arXiv preprint arXiv:2403.05034 (2024).
- [11] Y.-C. Cheng, H.-Y. Lee, S. Tuyakov, A. Schwing, L. Gui, SDFusion: Multimodal 3d shape completion, reconstruction, and generation, in: CVPR, 2023.
- [12] A. Gupta, W. Xiong, Y. Nie, I. Jones, B. Oğuz, 3dgen: Triplane latent diffusion for textured mesh generation (2023). arXiv:2303.05371. URL https://arxiv.org/abs/2303.05371
- [13] Z. Liu, Y. Feng, M. J. Black, D. Nowrouzezahrai, L. Paull, W. Liu, Meshdiffusion: Score-based generative 3d mesh modeling, in: International Conference on Learning Representations, 2023. URL https://openreview.net/forum?id=0cpM2ApF9p6

- [14] H. Jun, A. Nichol, Shap-e: Generating conditional 3d implicit functions (2023). arXiv:2305.02463.
   URL https://arxiv.org/abs/2305.02463
- [15] M. Li, Y. Duan, J. Zhou, J. Lu, Diffusion-sdf: Text-to-shape via voxelized diffusion (2023). arXiv:2212.03293.
   URL https://arxiv.org/abs/2212.03293
- [16] X. Zeng, A. Vahdat, F. Williams, Z. Gojcic, O. Litany, S. Fidler, K. Kreis, Lion: Latent point diffusion models for 3d shape generation (2022). arXiv:2210.06978. URL https://arxiv.org/abs/2210.06978
- [17] J. Ho, A. Jain, P. Abbeel, Denoising diffusion probabilistic models (2020). arXiv:2006.11239.
   URL https://arxiv.org/abs/2006.11239
- [18] O. Ronneberger, P. Fischer, T. Brox, U-net: Convolutional networks for biomedical image segmentation (2015). arXiv:1505.04597. URL https://arxiv.org/abs/1505.04597
- [19] Y. Hong, K. Zhang, J. Gu, S. Bi, Y. Zhou, D. Liu, F. Liu, K. Sunkavalli, T. Bui, H. Tan, Lrm: Large reconstruction model for single image to 3d, arXiv preprint arXiv:2311.04400 (2023).
- [20] A. Vaswani, N. Shazeer, N. Parmar, J. Uszkoreit, L. Jones, A. N. Gomez, L. Kaiser, I. Polosukhin, Attention is all you need (2023). arXiv:1706.03762. URL https://arxiv.org/abs/1706.03762
- [21] M. Liu, C. Xu, H. Jin, L. Chen, M. Varma T, Z. Xu, H. Su, One-2-3-45: Any single image to 3d mesh in 45 seconds without per-shape optimization, Advances in Neural Information Processing Systems 36 (2024).
- [22] J. Tang, Z. Chen, X. Chen, T. Wang, G. Zeng, Z. Liu, Lgm: Large multi-view gaussian model for high-resolution 3d content creation, arXiv preprint arXiv:2402.05054 (2024).
- [23] E. R. Chan, C. Z. Lin, M. A. Chan, K. Nagano, B. Pan, S. D. Mello, O. Gallo, L. Guibas, J. Tremblay, S. Khamis, T. Karras, G. Wetzstein,

- Efficient geometry-aware 3D generative adversarial networks, in: CVPR, 2022.
- [24] J. Gao, T. Shen, Z. Wang, W. Chen, K. Yin, D. Li, O. Litany, Z. Gojcic, S. Fidler, Get3d: A generative model of high quality 3d textured shapes learned from images, in: Advances In Neural Information Processing Systems, 2022.
- [25] J. Li, H. Tan, K. Zhang, Z. Xu, F. Luan, Y. Xu, Y. Hong, K. Sunkavalli, G. Shakhnarovich, S. Bi, Instant3d: Fast text-to-3d with sparse-view generation and large reconstruction model (2023). arXiv:2311.06214. URL https://arxiv.org/abs/2311.06214
- [26] P. Wang, H. Tan, S. Bi, Y. Xu, F. Luan, K. Sunkavalli, W. Wang, Z. Xu, K. Zhang, Pf-lrm: Pose-free large reconstruction model for joint pose and shape prediction (2023). arXiv:2311.12024. URL https://arxiv.org/abs/2311.12024
- [27] A. X. Chang, T. Funkhouser, L. Guibas, P. Hanrahan, Q. Huang, Z. Li, S. Savarese, M. Savva, S. Song, H. Su, J. Xiao, L. Yi, F. Yu, Shapenet: An information-rich 3d model repository (2015). arXiv:1512.03012. URL https://arxiv.org/abs/1512.03012
- [28] T. Wu, J. Zhang, X. Fu, Y. Wang, L. P. Jiawei Ren, W. Wu, L. Yang, J. Wang, C. Qian, D. Lin, Z. Liu, Omniobject3d: Large-vocabulary 3d object dataset for realistic perception, reconstruction and generation, in: IEEE/CVF Conference on Computer Vision and Pattern Recognition (CVPR), 2023.
- [29] M. Deitke, D. Schwenk, J. Salvador, L. Weihs, O. Michel, E. VanderBilt, L. Schmidt, K. Ehsani, A. Kembhavi, A. Farhadi, Objaverse: A universe of annotated 3d objects (2022). arXiv:2212.08051. URL https://arxiv.org/abs/2212.08051
- [30] D. P. Kingma, M. Welling, Auto-encoding variational bayes (2022). arXiv:1312.6114. URL https://arxiv.org/abs/1312.6114
- [31] L. Zhang, A. Rao, M. Agrawala, Adding conditional control to text-to-image diffusion models (2023).

- [32] B. Kerbl, G. Kopanas, T. Leimkühler, G. Drettakis, 3d gaussian splatting for real-time radiance field rendering, ACM Transactions on Graphics 42 (4) (July 2023).

  URL https://repo-sam.inria.fr/fungraph/3d-gaussian-splatting/
- [33] C.-H. Lin, J. Gao, L. Tang, T. Takikawa, X. Zeng, X. Huang, K. Kreis, S. Fidler, M.-Y. Liu, T.-Y. Lin, Magic3d: High-resolution text-to-3d content creation (2023). arXiv:2211.10440. URL https://arxiv.org/abs/2211.10440
- [34] Z. Wang, C. Lu, Y. Wang, F. Bao, C. Li, H. Su, J. Zhu, Prolificdreamer: High-fidelity and diverse text-to-3d generation with variational score distillation (2023). arXiv:2305.16213. URL https://arxiv.org/abs/2305.16213
- [35] C. Deng, C. M. Jiang, C. R. Qi, X. Yan, Y. Zhou, L. Guibas, D. Anguelov, Nerdi: Single-view nerf synthesis with language-guided diffusion as general image priors (2022). arXiv:2212.03267. URL https://arxiv.org/abs/2212.03267
- [36] A. Jain, B. Mildenhall, J. T. Barron, P. Abbeel, B. Poole, Zero-shot text-guided object generation with dream fields (2022).
- [37] Y. Chen, C. Zhang, X. Yang, Z. Cai, G. Yu, L. Yang, G. Lin, It3d: Improved text-to-3d generation with explicit view synthesis (2023). arXiv:2308.11473. URL https://arxiv.org/abs/2308.11473
- [38] L. Melas-Kyriazi, C. Rupprecht, I. Laina, A. Vedaldi, Realfusion: 360 reconstruction of any object from a single image, in: CVPR, 2023. URL https://arxiv.org/abs/2302.10663
- [39] G. Metzer, E. Richardson, O. Patashnik, R. Giryes, D. Cohen-Or, Latent-nerf for shape-guided generation of 3d shapes and textures (2022). arXiv:2211.07600. URL https://arxiv.org/abs/2211.07600
- [40] A. Raj, S. Kaza, B. Poole, M. Niemeyer, B. Mildenhall, N. Ruiz, S. Zada, K. Aberman, M. Rubenstein, J. Barron, Y. Li, V. Jampani, Dreambooth3d: Subject-driven text-to-3d generation, ICCV (2023).

- [41] J. Seo, W. Jang, M.-S. Kwak, J. Ko, H. Kim, J. Kim, J.-H. Kim, J. Lee, S. Kim, Let 2d diffusion model know 3d-consistency for robust text-to-3d generation, arXiv preprint arXiv:2303.07937 (2023).
- [42] B. Zhang, Y. Cheng, J. Yang, C. Wang, F. Zhao, Y. Tang, D. Chen, B. Guo, Gaussiancube: A structured and explicit radiance representation for 3d generative modeling (2024). arXiv:2403.19655. URL https://arxiv.org/abs/2403.19655
- [43] Y. Liang, X. Yang, J. Lin, H. Li, X. Xu, Y. Chen, Luciddreamer: Towards high-fidelity text-to-3d generation via interval score matching, arXiv preprint arXiv:2311.11284 (2023).
- [44] Z. Chen, F. Wang, Y. Wang, H. Liu, Text-to-3d using gaussian splatting (2024). arXiv:2309.16585. URL https://arxiv.org/abs/2309.16585
- [45] C. Wen, Y. Zhang, Z. Li, Y. Fu, Pixel2mesh++: Multi-view 3d mesh generation via deformation (2019). arXiv:1908.01491. URL https://arxiv.org/abs/1908.01491
- [46] R. Chen, Y. Chen, N. Jiao, K. Jia, Fantasia3d: Disentangling geometry and appearance for high-quality text-to-3d content creation (2023). arXiv:2303.13873.
  URL https://arxiv.org/abs/2303.13873
- [47] N. Wang, Y. Zhang, Z. Li, Y. Fu, W. Liu, Y.-G. Jiang, Pixel2mesh: Generating 3d mesh models from single rgb images (2018). arXiv:1804.01654. URL https://arxiv.org/abs/1804.01654
- [48] O. Michel, R. Bar-On, R. Liu, S. Benaim, R. Hanocka, Text2mesh: Text-driven neural stylization for meshes (2021). arXiv:2112.03221. URL https://arxiv.org/abs/2112.03221
- [49] N. Mohammad Khalid, T. Xie, E. Belilovsky, T. Popa, Clip-mesh: Generating textured meshes from text using pretrained image-text models, in: SIGGRAPH Asia 2022 Conference Papers, SA '22, ACM, 2022, p. 1–8. doi:10.1145/3550469.3555392.
  URL http://dx.doi.org/10.1145/3550469.3555392

- [50] G. Qian, J. Mai, A. Hamdi, J. Ren, A. Siarohin, B. Li, H.-Y. Lee, I. Skorokhodov, P. Wonka, S. Tulyakov, B. Ghanem, Magic123: One image to high-quality 3d object generation using both 2d and 3d diffusion priors (2023). arXiv:2306.17843. URL https://arxiv.org/abs/2306.17843
- [51] R. Rombach, A. Blattmann, D. Lorenz, P. Esser, B. Ommer, High-resolution image synthesis with latent diffusion models (2022). arXiv:2112.10752. URL https://arxiv.org/abs/2112.10752
- [52] R. Rombach, A. Blattmann, D. Lorenz, P. Esser, B. Ommer, High-resolution image synthesis with latent diffusion models (2022). arXiv:2112.10752. URL https://arxiv.org/abs/2112.10752
- [53] K. He, X. Zhang, S. Ren, J. Sun, Deep residual learning for image recognition (2015). arXiv:1512.03385. URL https://arxiv.org/abs/1512.03385
- [54] Z. Wu, S. Song, A. Khosla, F. Yu, L. Zhang, X. Tang, J. Xiao, 3d shapenets: A deep representation for volumetric shapes (2015). arXiv:1406.5670. URL https://arxiv.org/abs/1406.5670
- [55] T. Shen, J. Munkberg, J. Hasselgren, K. Yin, Z. Wang, W. Chen, Z. Gojcic, S. Fidler, N. Sharp, J. Gao, Flexible isosurface extraction for gradient-based mesh optimization, ACM Trans. Graph. 42 (4) (jul 2023). doi:10.1145/3592430. URL https://doi.org/10.1145/3592430
- [56] L. Yang, B. Kang, Z. Huang, X. Xu, J. Feng, H. Zhao, Depth anything: Unleashing the power of large-scale unlabeled data, in: CVPR, 2024.
- [57] L. Yang, B. Kang, Z. Huang, Z. Zhao, X. Xu, J. Feng, H. Zhao, Depth anything v2, arXiv:2406.09414 (2024).
- [58] S. Laine, J. Hellsten, T. Karras, Y. Seol, J. Lehtinen, T. Aila, Modular primitives for high-performance differentiable rendering, ACM Transactions on Graphics 39 (6) (2020).

- [59] X. Qin, Z. Zhang, C. Huang, M. Dehghan, O. Zaiane, M. Jagersand, U2-net: Going deeper with nested u-structure for salient object detection, Vol. 106, 2020, p. 107404.
- [60] C. T. Loop, Smooth subdivision surfaces based on triangles, 1987. URL https://api.semanticscholar.org/CorpusID:116150707
- [61] Z. He, T. Wang, OpenIrm: Open-source large reconstruction models, https://github.com/3DTopia/OpenLRM (2023).
- [62] L. Downs, A. Francis, N. Koenig, B. Kinman, R. Hickman, K. Reymann, T. B. McHugh, V. Vanhoucke, Google scanned objects: A high-quality dataset of 3d scanned household items (2022). arXiv:2204.11918. URL https://arxiv.org/abs/2204.11918
- [63] A. Ramesh, M. Pavlov, G. Goh, S. Gray, C. Voss, A. Radford, M. Chen, I. Sutskever, Zero-shot text-to-image generation (2021). arXiv:2102.12092. URL https://arxiv.org/abs/2102.12092
- [64] A. Nichol, H. Jun, P. Dhariwal, P. Mishkin, M. Chen, Point-e: A system for generating 3d point clouds from complex prompts (2022). arXiv:2212.08751. URL https://arxiv.org/abs/2212.08751
- [65] Y.-C. Guo, Y.-T. Liu, R. Shao, C. Laforte, V. Voleti, G. Luo, C.-H. Chen, Z.-X. Zou, C. Wang, Y.-P. Cao, S.-H. Zhang, threestudio: A unified framework for 3d content generation, https://github.com/threestudio-project/threestudio (2023).
- [66] A. Radford, J. W. Kim, C. Hallacy, A. Ramesh, G. Goh, S. Agarwal, G. Sastry, A. Askell, P. Mishkin, J. Clark, G. Krueger, I. Sutskever, Learning transferable visual models from natural language supervision (2021). arXiv:2103.00020. URL https://arxiv.org/abs/2103.00020
- [67] Z. Wang, A. C. Bovik, H. R. Sheikh, E. P. Simoncelli, Image quality assessment: from error visibility to structural similarity, IEEE Transactions on Image Processing 13 (2004) 600-612. URL https://api.semanticscholar.org/CorpusID:207761262

[68] R. Zhang, P. Isola, A. A. Efros, E. Shechtman, O. Wang, The unreasonable effectiveness of deep features as a perceptual metric (2018). arXiv:1801.03924.

 ${\rm URL\ https://arxiv.org/abs/1801.03924}$